Acoustic sensing as a tool for brain tumor diagnostics

Melanie E. M. Stamp, Friederike Liesche Starnecker, Tina Schaller, Peter Baumgarten, Nadine Lilla, Dorothee Mielke, David Collins

Angaben zur Veröffentlichung / Publication details:

Stamp, Melanie E. M., Friederike Liesche-Starnecker, Tina Schaller, Peter Baumgarten, Nadine Lilla, Dorothee Mielke, and David Collins. 2026. "Acoustic sensing as a tool for brain tumor diagnostics." *Advanced Sensor Research* 5 (2): e00002. https://doi.org/10.1002/adsr.202600002.

Advanced Sensor Research

ADVANCED SENSOR RESEARCH Open Access

www.advsensorres.com

RESEARCH ARTICLE OPEN ACCESS

Acoustic Sensing as a Tool for Brain Tumor Diagnostics

Melanie E. M. Stamp[1,2] | Friederike Liesche-Starnecker[3,4,5] | Tina Schaller[4] | Peter Baumgarten[6] | Nadine Lilla[6] | Dorothee Mielke[6] | David Collins[1,2]

[1]Department of Biomedical Engineering, Faculty of Engineering and IT, The University of Melbourne, Parkville, Australia | [2]Graeme Clark Institute for Biomedical Engineering, Melbourne, Australia | [3]Department of Neuropathology, Pathology, Medical Faculty, University of Augsburg, Augsburg, Germany | [4]Pathology, Medical Faculty, University of Augsburg, Augsburg, Germany | [5]Institut of Neuropathology, Ulm University Hospital, Medical Faculty, Ulm University, Ulm, Germany | [6]Department of Neurosurgery, University Hospital Augsburg, University of Augsburg, Germany

Correspondence: Melanie E. M. Stamp (melanie.stamp@unimelb.edu.au) | David Collins (david.collins@unimelb.edu.au)

Received: 7 January 2026 | **Revised:** 15 January 2026 | **Accepted:** 26 January 2026

Keywords: acoustic biosensing | brain tumour diagnostics | mechanical property mapping | tissue stiffness characterization | tumor microenvironment

ABSTRACT

Accurate intraoperative identification of brain tumor margins remains a major challenge in neurosurgery. Tumors often differ from healthy brain tissue in their mechanical properties, such as stiffness and viscoelasticity, yet current imaging methods provide limited real-time mechanical feedback during surgery. In this study, the use of acoustic sensing based on surface acoustic wave (SAW) actuators to distinguish between non-neoplastic brain tissue, primary brain tumors, and metastatic tumors based on their acoustic properties is investigated. Tissue samples are measured ex vivo, and attenuation is analyzed as a function of mass and stiffness. Results showed clear, consistent trends, where non-neoplastic tissues exhibit increased acoustic attenuation, metastatic tumors exhibited intermediate attenuation, and primary tumors showed the lowest attenuation, reflecting increasing stiffness across these tissue types. These findings align with previously reported mechanical properties from techniques such as magnetic resonance elastography and microindentation, where acoustic/SAW based methodologies have significant potential advantages in throughput, cost-effectiveness and integrability with other techniques. Accordingly, this work demonstrates that SAW sensing enables reliable sensitivity to biomechanical differences between tissue types, supporting its potential as a real-time, non-invasive tool for intraoperative tumor detection.

1 | Introduction

Central nervous system (CNS) malignancies pose a significant global health challenge. Their location in the brain and spinal cord makes them particularly devastating, as even non-malignant tumors can disrupt critical neurological functions and lead to disability and cognitive decline [1–3]. Surgical resection remains a key determinant of outcomes, with greater tumor removal linked to improved survival [4–6]. However, despite advances in neurosurgery and imaging, recurrence rates remain high. For example, glioblastoma (GBM) recurs locally in ~ 30% of patients within a year, often due to residual microscopic cells undetected during surgery [1, 7, 8].

Accurately distinguishing tumor margins from healthy tissue remains a significant challenge. Traditional intraoperative imaging techniques have provided neurosurgeons with essential guidance yet presents limitations that hinder the full realization of precise tumor resection. Magnetic resonance imaging (MRI) provides high-resolution planning but is limited intraoperatively by logistical barriers and brain shift and the need for specialized intraoperative MRI suites [2, 9]. Other approaches, which rely on preoperative imaging, become increasingly inaccurate as brain tissue deforms during surgery. Fluorescence-guided surgery enhances tumor visualization but suffers from shallow penetration and variable uptake, leading to false negatives [5–7, 10], leading to false negatives. Ultrasound offers real-

time imaging but with poor resolution [11, 12]. These methods primarily provide structural or molecular data, overlooking biomechanical properties such as stiffness and viscoelasticity—features that often differ markedly between tumors and healthy brain. Tumor tissue often exhibits increased stiffness or rigidity due to proliferation of abnormal cells and deposition of dense extracellular matrix components such as collagen [18]. Surgeons frequently rely on subjective haptic feedback, which varies with experience [8, 13–16]. These alterations result from cellular abnormalities, inflammation, tissue damage, oedema or accumulation of abnormal proteins [17]. While this skill, developed through years of practice, remains essential, it is inherently subjective, and can vary based on the surgeon's experience and tumor characteristics.

Emerging research highlights the diagnostic potential of biomechanics—such as stiffness and viscoelasticity. For instance, GBM exhibits heterogeneous stiffness due to regions of necrosis and vascular proliferation, while meningiomas tend to be uniformly stiffer than surrounding tissue [8, 13, 14, 18]. Recognizing these differences has driven the development of techniques to measure tissue stiffness, providing neurosurgeons with new tools to improve tumor delineation.

Magnetic Resonance Elastography (MRE) has shown promise as a non-invasive preoperative method for mapping brain tissue stiffness. Duhon et al. (2024) demonstrated that MRE could distinguish between vestibular schwannomas and meningiomas, linking stiffer tumors to more complex resections, were tumor stiffness correlated with microenvironmental changes, like increased hyaluronic acid and macrophage infiltration [8]. However, MRE is limited to preoperative use and lacks real-time intraoperative feedback. Shear Wave Elastography (SWE) offers real-time stiffness mapping but is hindered by anatomical complexity, while micro-indentation provides high-resolution direct measurements yet is invasive and limited in scope [14]. However, SWE is limited by anatomical complexity and skull interference. Conversely micro indentation, though invasive, allows for high resolution direct stiffness measurements, where Skambath et al. found that it aligned with surgeons' tactile assessments, though lacks the precision needed to distinguish all tumor types [13]. Computational models further support biomechanical assessments by mapping stiffness across brain regions and linking ECM alterations to tumour rigidity. Budday et al. mapped stiffness and viscoelasticity across brain regions, noting that white matter is generally stiffer than grey matter [16]. Kren et al. highlighted increased stiffness in glioblastomas due to ECM alterations, achieving 83% sensitivity and 85% precision in tumor classification [18]. Similarly, Hinrichsen et al. used hyper elastic modelling to capture region-specific brain mechanics, aiding surgical planning [19]. Collectively, these studies emphasize the diagnostic value of biomechanical assessments in brain tumor surgery. While MRE and SWE provide valuable stiffness data, challenges remain in achieving consistent intraoperative application. Integrating biomechanical insights with conventional imaging thus presents a compelling opportunity for improving tumor localization, guiding resections, and enhancing surgical outcomes.

Surface Acoustic Wave (SAW) sensing has the potential to enable real-time assessment of tissue stiffness during surgery, where SAW-based approaches have been previously demonstrated utility for highly sensitive chemical, biosensor and pressure sensing applications [20]. Beyond sensing, SAW can also manipulate biological systems, enhancing microscale transport [21], probing cell adhesion under shear stress [22, 23], and stimulating directed cell migration in wound healing [24]. These findings highlight the dual role of SAW as both a diagnostic and bioactive technology with clear translational potential. SAW generate high-frequency waves that are highly sensitive to stiffness, density, and viscoelasticity of materials in contact with the sensor. These interactions cause changes in wave propagation that are a function of the material's mechanical properties [25, 26]. This sensitivity makes SAW technology potentially valuable for distinguishing biological tissues with varying mechanical profiles. Several studies have demonstrated the effectiveness of acoustic sensing in capturing complex mechanical behaviors, highlighting the versatility of SAW devices in detecting subtle changes in viscoelastic properties in materials [27]. Wu et al. demonstrated a logarithmic relationship between insertion loss and wave attenuation in shear horizontal SAW (SH-SAW) devices, directly linking increased cell viscosity to greater damping effects [28, 29]. Ruland et al. explored the impact of material characteristics such as swelling ratio, thickness, and modulus on wave attenuation in hydrogels, confirming linear and exponential trends in acoustic responses relative to material stiffness [30, 31]. Our recent work has also shown that mass loading leads to a linear increase in wave attenuation, while increased material stiffness results in an exponential decrease in attenuation [32]. These characteristics make SAW technology well-suited for distinguishing biological tissues with varying mechanical profiles.

In this study, we explore the potential of SAW sensing for differentiating between primary brain tumors, metastatic tumors, and non-neoplastic brain tissue based on their mechanical signatures. Normalizing attenuation data against controls allowed us to separate stiffness effects from mass influences. Results show primary tumors exhibit lower attenuation (stiffer), metastases intermediate, and healthy tissue the highest. These findings align with established biomechanical profiles of brain tissues and tumors and demonstrate the potential of SAW technology as a real-time diagnostic tool. By providing immediate stiffness feedback, SAW could complement imaging, improve tumor delineation, and enhance surgical precision and patient outcomes.

2 | Methods and Materials

An abstract overview of the experimental workflow is shown in Figure 1a. Freshly resected brain tissue is obtained during neurosurgery, followed by surface acoustic wave (SAW) sensing to record acoustic attenuation signals. After acoustic measurements, tissue samples undergo histopathological analysis to classify them as non-neoplastic, primary tumor, or metastatic tumor. The acoustic and pathological data are then combined to determine attenuation as a function of tissue weight and pathology, enabling tissue-specific mechanical profiling across healthy and diseased brain regions

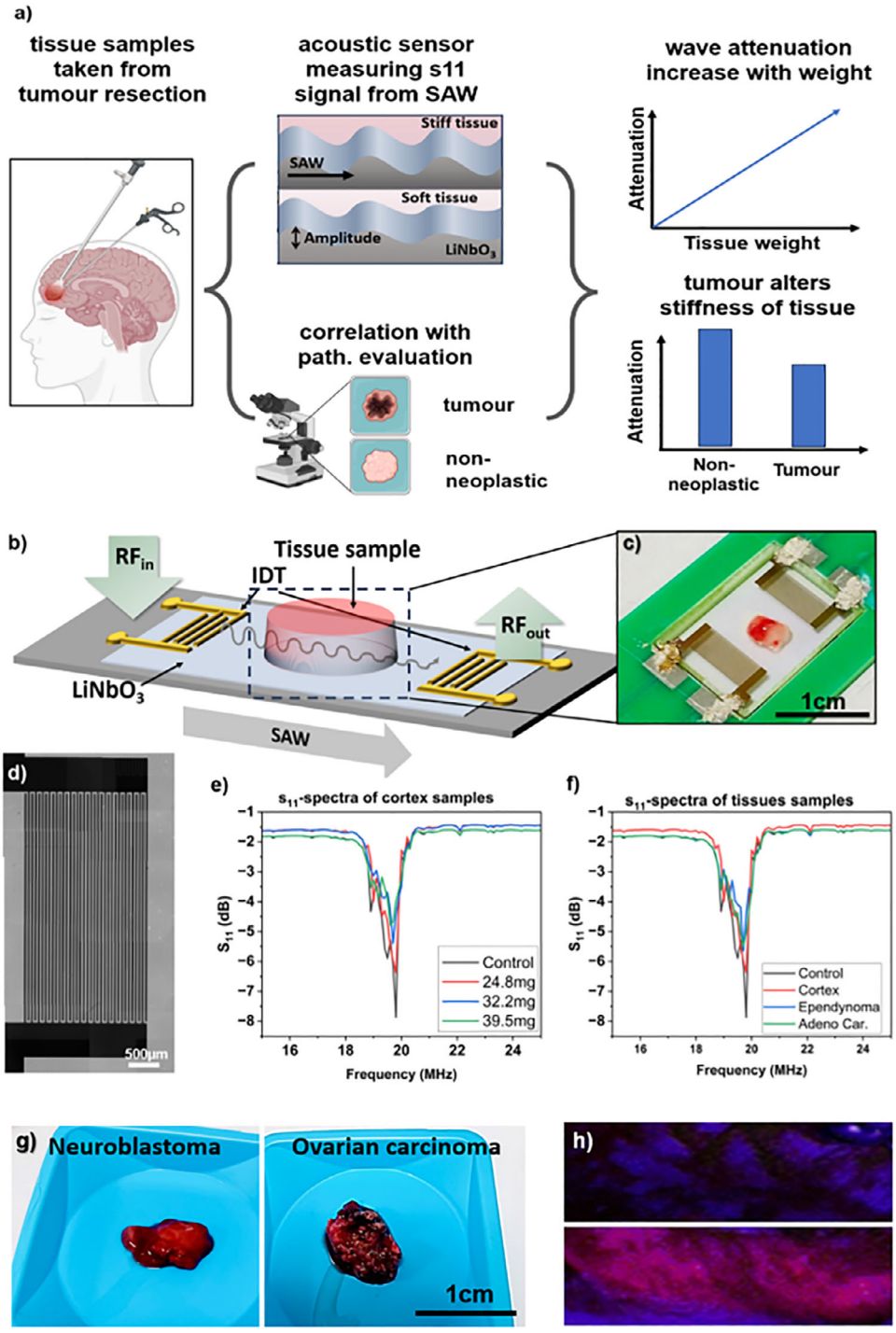

FIGURE 1 | (a) Abstract graphical overview of the experimental workflow. Brain tissue is obtained during neurosurgery, followed by surface acoustic wave (SAW) sensing to record acoustic attenuation signals. Subsequent histopathological analysis classifies samples as non-neoplastic, primary tumor, or metastatic tumor. Acoustic and pathological data are combined to determine attenuation as a function of tissue weight and pathology. (b) schematic of acoustic sensors chips. A RF signal is generated at the left IDT (RFin), travelling along the LiNbO3 surface and read out at the right IDT (RFout). Tumor tissue in sound path of the SAW absorbs parts of the waves energy resulting in a detectable wave attenuation. c) image of SAW-chip with tumor tissue, (c) two types of tumor tissue assessed, (d) Light microscopic image of the fabricated interdigital transducers, illustrating the electrode geometry (minimum feature size ≈ 25 µm). (e) S11 reflection spectra (15–25 MHz) showing the resonance minimum at approximately 19.8 MHz for the unloaded control and three cortex tissue samples of different weights, demonstrating mass-loading effects on acoustic attenuation. (f) S11 spectra for tissue samples of approximately equal weight obtained from three different patients: non-neoplastic cortex tissue, ependymoma, and adenocarcinoma, enabling direct comparison of acoustic responses across different pathologies. (g) tissue samples of Neuroblastoma as primary tumor and Ovarian carcinoma as metastatic tumor. (h) tumor tissue without (top) and with (bottom) fluorescence marker showing infiltrated areas of glioblastoma, taken from Bettag et al. [46].

2.1 | Acoustic Sensor Design

Here Rayleigh-mode SAW devices were developed for non-invasive mechanical characterization of GelMA hydrogels. The devices utilize piezoelectric128° Y-cut lithium niobate ($LiNbO_3$) wafers (20 mm × 15 mm × 0.5 mm) as the substrate material, chosen due to its high coupling coefficient and generation of out-of-plane wavefront displacements whose energy is concentrated at the substrate surface. Interdigital transducers (IDTs) were patterned on this material using standard photolithography (Photoresist AZ nLOF 2035, ABM UV Flood Light Source, SUSS MA6) and deposited via electron-beam evaporation (Intlvac Nanochrome II) with a Ti/Au/Ti layer thickness of 15/60/15 nm, followed by a 200 nm SiO_2 passivation layer applied using PECVD (Oxford Instruments PLASMALAB 100) at 250°C. The IDTs were designed with a periodicity of $\lambda_{SAW} = 200$ µm, corresponding to a Rayleigh-mode SAW resonance frequency of 19.85 MHz, 18 finger pairs (Figure 1d), and an aperture of 8 mm was chosen to optimize wave-material interaction. The delay line was set to 8 mm, ensuring adequate wave propagation while minimizing energy loss. SAW devices were mounted on a custom PCB holder and connected to a NanoVNA-H4 network analyzer (Seesii, China), to record S11 reflection loss (Figure 1e,f) across a frequency range of 15–25 MHz using NanoVNA-Saver software for data acquisition and processing. Further descriptions of sensor fabrication and calibration are reported in previous work [32].

2.2 | Tissue Resection and Preparation

Brain tumor samples were obtained from patients undergoing neurosurgery at the University Hospital Augsburg, Department for Neurosurgery, Germany in July 2024, and they or their legal guardians gave informed written consent in accordance with the local ethic guidelines. Non-neoplastic brain tissue was retrieved from autopsies taken place in July 2024 at the University Hospital Augsburg, Department for Pathology, Germany, ensuring a diverse dataset for acoustic sensing analysis. Non neoplastic brain samples were collected shortly after death to maintain structural integrity, and tumor tissues obtained directly from patients undergoing surgical resection. All procedures followed ethical guidelines for human tissue research and were approved by the institutional ethics committee (LMU Muenchen under ethics approval number 24–0338). Non-neoplastic Brain Samples were collected from post-mortem donors within 12 h after the official time of death due to cardiac arrest to ensure minimal degradation of mechanical properties. Tumor Tissue Samples were obtained from patients undergoing neurosurgical procedures, categorized into primary tumors and metastatic tumors as follows:

Primary Tumors: glioblastoma, astrocytoma, schwannoma, neuroblastoma, plexus papilloma, pituitary adenoma.

Metastatic Tumors: adenocarcinoma (not otherwise specified), mammary carcinoma, ovarian carcinoma, neuroendocrine carcinoma.

The plexus papilloma was located in the fourth ventricle, attached to the plexus choroideus and extended to the right cerebellum. The tumor tissue was perceived as rather soft. Although the tumor was devascularized endovascularly with fibrin glue prior to surgery, bipolar coagulation was frequently used during the operation to stop bleeding. This may have influenced mechanical properties of the collected tumor tissue for further analysis.

The supratentorial ependymoma was localized in the left cerebral lateral ventricle and the surgeon described the tumor tissue of coarse consistency.

The Schwannoma was located in the left cerebellopontine angle. Tumor tissue was described as elastic from the operating team.

The cerebral metastasis of a poorly differentiated neuroendocrine carcinoma was localized in the right parietal lobe. Tumor tissue was experienced to be largely coarse.

Parts of an intraspinal poorly differentiated, stroma-poor neuroblastoma were resected from the lumbar extradural space. Tumor consistency was described as elastic.

The glioblastoma was a recurrent tumor and IDH wild type. It was located in the temporal lobe and surgeons described the resection of a rather elastic tumor tissue.

The cerebral metastasis of an adenocarcinoma of the lung (NSCLC) was localized in the right precentral area. Unfortunately, there was no further details about the intraoperative tissue characteristics of the tumor available.

The cerebellar metastasis of a breast carcinoma was excised out of the left cerebellar tonsil. Tumor consistency was described as coarse.

The infratentorial metastasis of an ovarian carcinoma was located in the fourth ventricle and cerebellar. Tumor tissue was found to be out of elastic consistency.

Parts of a somatotrophic pituitary adenoma were resected out of the pituitary gland. The tumor tissue was described as liquid.

Table 1 summarizes all tumor tissue locations and intraoperatively described tumor tissue characteristics.

A portion of the mammary carcinoma tissue was preserved in 4% formalin. The potential impact of tissue preservation on mechanical properties is explicitly considered in the analysis and discussed below. All other tumors and healthy brain tissues were frozen to −80°C without fixation or chemical treatment, immediately upon extraction from the patient or donor.

2.3 | Tissue Analysis

2.3.1 | Acoustic Analysis

Frozen tissue samples were divided into smaller pieces of varying sizes, ranging from approximately 30 to 100 mm^3, depending on the size of the available tumor material. Each sample was thawed and weighed prior to analysis to generate statistical data and ensure a mass load measurement specific to each tumor type and non-neoplastic brain region (weights detailed in Table 1). The experimental set-up is depicted in Figure 1b) with a picture of the

TABLE 1 | Tissue sample location, weight and attenuation values.

Tissue	Location	IntraOP consistency	Ave. Weight (mg)	Slope	Attenuation	Pearson R
Non-neoplastic tissue*1				—	0.808	
Cerebellum			26.7	−8.462 ± 1.593	0.782 ± 0.041	0.88
Cortex			32.2	−7.698 ± 0.280	0.802 ± 0.010	0.97
Pons			35.1	−8.285 ± 0.343	0.838 ± 0.011	0.96
Medulla			32.3	−5.360 ± 0.174	0.862 ± 0.006	0.96
Spinal cord			61.3	−3.181 ± 0.195	0.918 ± 0.008	0.95
Average Primary*2					0.874	
Plexus Papilloma	IV. ventricle, plexus, right cerebellar	soft (embolization fibrin glue)	6.6	−6.496 ± 0.771	0.833 ± 0.134	0.77
Ependymoma	left cerebral lateral ventricle	coarse	27.5	−5.424 ± 0.224	0.861 ± 0.006	0.99
Schwannoma	left cerebellopontine angle	elastic	25.7	−5.476 ± 0.201	0.859 ± 0.006	0.98
Neuroblastoma	lumbal extradural	elastic	13.5	−3.607 ± 0.524	0.907 ± 0.014	0.96
Glioblastoma	temporal	elastic	27.4	−5.190 ± 0.522	0.867 ± 0.015	0.94
Pituitary adenoma	Pituitary gland	liquid	11.9	−10.882 ± 0.792	0.720 ± 0.121	0.98
Average Metastasis*3					0.868	
Neuroendocrine	right parietal lobe	coarse	41.53	−3.232 ± 0.141	0.917 ± 0.004	0.99
Adenocarcinoma of the lung	pre-central right	—	19.5	−5.775 ± 0.296	0.851 ± 0.008	0.97
Breast car.	left cerebellar tonsil	coarse	7.8	−6.117 ± 0.923	0.843 ± 0.024	0.96
Breast car. formalin	left cerebellar tonsil	coarse	19.9	−1.169 ± 0.131	0.969 ± 0.004	0.96
Ovarian car.	IV. ventricle, cerebellar	elastic	22.9	−5.351 ± 0.794	0.862 ± 0.021	0.97

Slope measured from attenuation over weight graphs, calculated attenuation at all tissue average weight of 25.7 mg, Pearson's R, and intra operative consistency described by the surgeon.

*1Average non-neoplastic brain attenuation includes only soft matter (Cerebellum, Cortex, Pons).

*2Average Primary tumor excludes Plexus Papilloma and Pituitary adenoma, as their consistency has been altered/described as fluid.

*3Average metastasis excludes brain carcinoma in formalin due to tissue preparation.

device in Figure 1c). A sample is placed in the middle of the SAW chip between both IDTs. All tissue samples were positioned centrally between the interdigital transducers to ensure consistent interaction with the propagating surface acoustic wave. Sample placement was visually verified before each measurement, and the same positioning protocol was applied across all experiments to minimize geometric variability. This standardized approach ensures that observed attenuation differences primarily reflect tissue mechanical properties rather than placement effects.

As the wave travels along the surface part of its energy is absorbed by the material on top resulting in a detectable wave attenuation in reflection s11 and transmission s21 signal, as well as a frequency shift. In our experiments, acoustic sensing, S_{11} reflection loss and frequency response were recorded for each sample to assess variations in wave attenuation. To provide direct electrical characterization of the SAW device, S11 reflection spectra were recorded over a frequency range of 15–25 MHz using the network analyzer. Representative frequency response plots are shown in Figure 1e,f. Figure 1e displays the unloaded control measurement (no tissue present) together with three cortex tissue samples of different weights. A clear resonance minimum is observed at approximately 19.8 MHz, corresponding to the designed SAW wavelength of 200 μm, as described above. Increasing sample mass results in progressive changes in reflection amplitude, demonstrating the expected mass-loading effect on the propagating surface acoustic wave. Figure 1f shows S11 spectra for tissue samples of approximately equal weight obtained from three different patients: non-neoplastic cortex tissue, ependymoma, and adenocarcinoma. These tumor types were selected as they originated from cortical regions, enabling a direct comparison of acoustic responses for samples of similar mass but differing pathology. This dataset highlights differences in attenuation behavior arising from tissue-specific mechanical properties rather than sample mass.

To maintain consistency and minimize measurement artifacts, a control test was conducted before and after each tissue measurement, involving an initial baseline measurement with no material placed on the sensor, followed by a sample test, another

control test, and then a second sample test. This alternating control-sample-control sequence ensured that any environmental or instrumental drift was accounted for in the data analysis. Between tests, the SAW sensor chip was cleaned with an alcohol wipe and thoroughly dried to prevent biological residue build-up and ensure reproducibility across measurements.

2.3.2 | Histological Analysis

Sample Preservation: After acoustic measurements, tissue samples were collected and stored frozen at −80°C. Samples were thawed, then fixed in 4% formalin for a minimum of six hours and then embedded into paraffin to facilitate sectioning for histological analysis. Formalin-fixed-paraffin-embedded (FFPE) samples were cut into 2 µm-thin sections and stained with hematoxylin and eosin (HE) following standard protocols. The HE-stained sections were examined under a light microscope to assess the representative nature of the sample, tissue morphology, structural integrity, and the presence of any artifacts resulting from the embedding process. Representative images were captured using a digital slide scanner (PANNORAMIC II by 3DHISTECH) for further evaluation. However, the definitive histopathological diagnosis was established based on the specimens obtained for diagnostic purposes.

2.4 | Data Analysis and Fitting Approach

To quantify the relationship between wave attenuation and tissue stiffness, we adopt a mathematical framework whereby a mass load leads to a linear increase in wave attenuation both theoretically and experimentally (Stamp, 2025). This principle is described by:

$$\alpha = \frac{2\pi f}{v_p} \times \frac{m}{\rho}, \tag{1}$$

where α is the attenuation coefficient, f is the wave frequency, v_p is the phase velocity, and m is the mass load per unit area. This equation establishes a direct linear dependence of attenuation on mass load, meaning that heavier tissue samples induce stronger attenuation effects in the SAW system.

To account for these mass-dependent variations, we normalize all attenuation measurements by dividing them by the baseline (control) measurement, where no material was placed on the SAW sensor. This normalization ensured that the maximum reflection signal corresponded to 1 (i.e., no sample present), providing a relative attenuation scale for all tumor and healthy brain tissues. For each tissue type, attenuation (y-axis) was plotted as a function of sample weight (x-axis). A linear fit was applied to each dataset, enforcing the condition that at zero mass ($x = 0$), the normalized reflection should be 1 ($y = 1$). Resulting in:

$$y = mx + t \tag{2}$$

where m represents the attenuation slope, and the y-intercept t was fixed at 1 to maintain consistency with the normalized control. The mean weight across all samples was then used to calculate a normalized attenuation value for each tissue, allowing a direct comparison of attenuation effects across different tissue types. This approach eliminates mass-related bias and enables a clearer evaluation of the intrinsic acoustic properties of each tumor and non-neoplastic brain region. Similar mathematical modelling approaches using autoregressive methods have been successfully applied in high-resolution acoustic studies of biological tissues to extract speed-of-sound and attenuation values, even in thin cryosections [33]. Furthermore, our standardized fitting technique aligns with previous studies that highlight the potential of acoustic parameters in real-time intraoperative applications. For instance, acoustic feedback mechanisms have already been shown to enhance tumor boundary recognition with lower infrastructure demands compared to intraoperative MRI [34]. These findings reinforce the translational value of our approach for surgical guidance.

3 | Results and Discussion

Two key analyses were conducted to evaluate the acoustic properties of brain tumor tissues and healthy brain regions. The first highlights the relationship between tissue weight and acoustic attenuation, demonstrating the impact of mass loading on acoustic output across different tissue types. The second utilizes this data to normalize and compare acoustic attenuation across tumor and healthy tissue types.

3.1 | Acoustic Attenuation as a Function of Weight

Prior to quantitative fitting, the raw electrical response of the SAW device was examined to visualize mass-loading effects directly. Figure 1e shows the S11 reflection spectra for the unloaded control and three cortex samples of increasing weight. A pronounced resonance minimum is observed at approximately 19.8 MHz, corresponding to the designed SAW wavelength of 200 µm. With increasing tissue mass, the depth of the reflection minimum progressively decreases, indicating increased acoustic attenuation. Notably, the resonance frequency itself remains largely unchanged, confirming that mass loading primarily affects signal amplitude rather than inducing a measurable frequency shift in this experimental regime. This validates the use of attenuation depth as the primary sensing parameter and supports the linear mass–attenuation relationship quantified in Figure 2.

Figure 2 depicts the relationship between normalized reflection and tissue weight across healthy brain tissue, primary tumors, and metastatic tumors. Across all tissue types, a linear relationship between weight and reflection is observed, supporting the theoretical framework outlined in Equation 1, which predicts that increased mass loading leads to a reduction in reflection due to greater acoustic attenuation. This trend is consistent with previous studies investigating wave propagation in biological tissues, where mass load effects contribute significantly to energy dissipation [27]. Table 1 lists data for the individual tissue types.

3.1.1 | Non-Neoplastic Brain Tissue

The autoptic retrieved non-neoplastic brain tissue (Figure 2a) exhibit high attenuation and lower reflection, consistent with

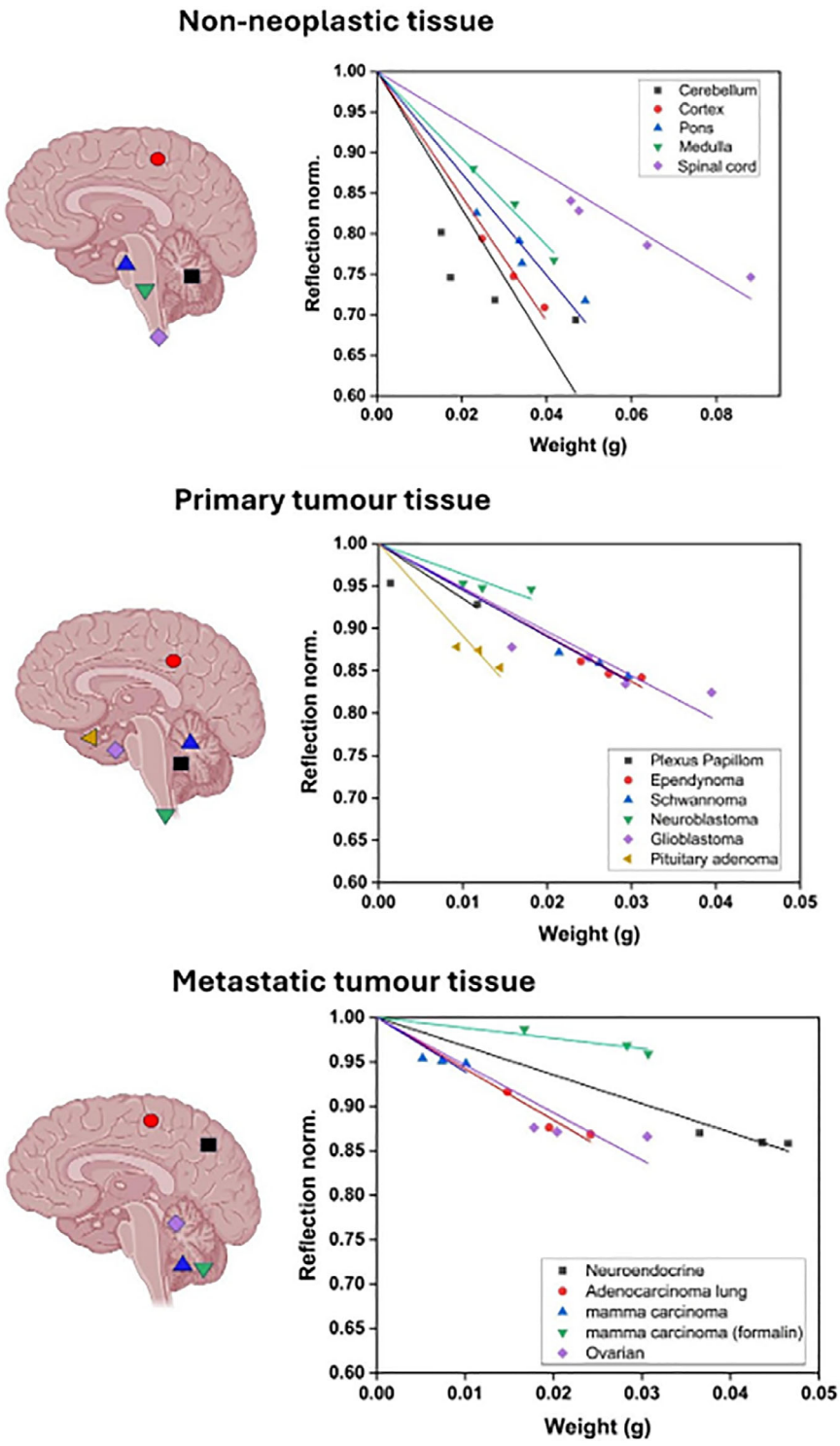

FIGURE 2 | Acoustic attenuation as a function of weight for different tissue types. The left panels illustrate the anatomical locations of the tested tissue samples in the brain and spinal cord. The right panels show the normalized reflection as a function of sample weight for (a) healthy brain tissues, (b) primary brain tumors, and (c) metastatic tumors. A clear linear relationship between weight and attenuation is observed across all tissue types, with steeper slopes indicating higher attenuation and softer tissue properties. Non-neoplastic tissues exhibit the highest attenuation, while primary and metastatic tumors demonstrate reduced attenuation consistent with their increased stiffness.

their relatively soft, viscoelastic nature. The Cerebellum and Cortex display the steepest attenuation slopes (-8.462 ± 1.593 and -7.698 ± 0.280, respectively), suggesting significant wave absorption. The Pons and Medulla exhibit intermediate slopes (-8.285 ± 0.343 and -5.360 ± 0.174, respectively), reflecting their denser white matter composition, which has been shown to have a slightly higher stiffness than grey matter [19, 35]. The spinal cord demonstrates the lowest attenuation (slope: -3.181 ± 0.195), which is expected given its higher structural density. These findings align with previous mechanical studies that report

Young's modulus values for the cerebral cortex in the range of 0.5–1.5 kPa (low stiffness), whereas spinal tissue has a young modulus ranging from 2.0–3.5 kPa (higher stiffness) [16, 19].

3.1.2 | Primary Brain Tumor

The primary brain tumor samples (Figure 2b) demonstrate heterogeneous attenuation profiles, reflecting their diverse histological compositions. GBM exhibits a moderate attenuation slope (-5.190 ± 0.522), consistent with its high cellularity and dense extracellular matrix. Prior research has reported Young's modulus values ranging from 2–5 kPa for glioblastoma, confirming its increased stiffness compared to healthy brain tissue [18, 36]. Pituitary adenoma presents the steepest attenuation slope among primary tumors (-10.882 ± 0.792), indicating a significantly softer structure, which aligns with surgical haptic observations describing these tumors as "liquid-like". This is supported by mechanical studies showing Young's modulus values of pituitary adenomas in the range of 0.5–1.5 kPa, similar to soft grey matter [37]. Plexus papilloma, ependymoma, and schwannoma display intermediate slopes (-5.424 to -6.496), indicating moderate stiffness levels. Notably, the plexus papilloma sample treated preoperative devascularization with fibrin glue underwent coagulation treatment to control intraoperative bleeding, likely increasing its stiffness and affecting its attenuation profile. This is an important consideration, as coagulation and surgical manipulation can significantly alter the mechanical properties of tissues [8, 38]. Neuroblastoma shows the shallowest attenuation slope among primary brain tumors (-3.607 ± 0.524).

3.1.3 | Metastatic Tumors

The metastatic tumors (Figure 2c) display more uniform attenuation characteristics, but variations emerge based on tumor origin and preservation state. Fresh mammary carcinoma shows moderate attenuation (-6.117 ± 0.923), but its formalin-fixed counterpart exhibits drastically reduced attenuation (-1.169 ± 0.131), with the highest reflection value (0.969 ± 0.004), illustrating the stiffening effects of chemical fixation of tissue in formalin [39]. Adenocarcinoma of the lung and neuroendocrine carcinomas display moderate slopes with (-5.775 ± 0.296) and (-3.232 ± 0.141), indicating intermediate stiffness levels. Ovarian carcinoma, with a slope of (-5.351 ± 0.794) shows mechanical properties closer to those of healthy brain regions [13, 40].

3.2 | Acoustic Characteristics of Tumor vs Healthy Brain Tissue

To further explore the biomechanical differences between tumor tissues and non-neoplastic brain regions, the slopes derived from the weight-dependent attenuation analysis were used to calculate the normalized reflection for each tissue type at the mean tissue weight of 25.7 mg. This approach allowed for a direct comparison of acoustic attenuation across all tissue types, isolating the influence of tissue stiffness from the confounding effect of sample mass. Figure 1f illustrates the sensitivity of the SAW device to tissue-specific mechanical properties independent of mass. The spectra shown correspond to tissue samples of approximately equal weight obtained from three different patients: non-neoplastic cortex, ependymoma, and adenocarcinoma. Despite similar sample mass of approximately 24 mg, clear differences in attenuation depth are observed at the resonance frequency. Non-neoplastic cortex tissue exhibits the strongest attenuation, whereas the tumor samples show reduced damping, consistent with their increased stiffness. This demonstrates that the observed attenuation trends are not solely driven by mass loading but are also influenced by intrinsic tissue mechanical properties. These findings directly support the tissue-specific separation observed in Figure 3.

The results are summarized in Figure 3, where normalized reflection values for each tissue type are plotted alongside the average values for primary tumors, metastatic tumors, and non-neoplastic brain regions. For the comparative analysis of acoustic properties across tissue types, specific samples were excluded to ensure consistency and avoid confounding effects. From the non-neoplastic group, medulla and spinal cord samples were excluded as they inherently higher stiffness. Within the primary brain tumor group, the plexus papilloma (altered by intraoperative coagulation to control bleeding) and pituitary adenoma (noted for its liquid-like consistency) were excluded. In the metastatic group, the formalin-fixed breast carcinoma sample was excluded due to the immediate stiffening effect of chemical preservation. These exclusions enabled a more accurate comparison of intrinsic biomechanical properties across untreated, representative tissue types.

Non-neoplastic brain tissues exhibit the lowest reflection values, confirming higher attenuation due to their soft mechanical properties. The cerebellum and cortex demonstrate the greatest attenuation with (0.782 ± 0.041) and (0.802 ± 0.010), consistent with their highly deformable nature. In contrast, the spinal cord shows the highest reflection with (0.918 ± 0.008), reflecting its structurally denser and stiffer composition. These findings align with magnetic resonance elastography studies, where grey matter regions exhibit lower stiffness compared to white matter [16, 19], and shear wave elastography measurements, which confirm higher wave absorption in cortical regions [14, 41].

Primary brain tumors display significantly higher reflection values, confirming their greater stiffness relative to non-neoplastic brain tissue. GBM presents one of the highest reflection values (0.867 ± 0.015), aligning with studies by Kren et al., Khoonkoi et al., and Parkins et al. examining mechanical characteristics of GBM stiffness measurements reporting Young's modulus values between 2–6 kPa [18, 42, 43]. Pituitary Adenoma, despite being a tumor, exhibits low reflection with (0.720 ± 0.121), consistent with its soft, fluid-like structure with values near 1 kPa [37, 44]. Plexus papilloma with (0.833 ± 0.018), which underwent frequent coagulation treatment/preoperative devascularization with fibrin glue, presents an altered mechanical profile, likely due to pre- and surgical-induced stiffening, as previously observed in intraoperative shear wave elastography studies. Neuroblastoma demonstrates a reflection profile of (0.907 ± 0.014) similar to GBM, suggesting a high stiffness level, in agreement with previous studies by Harkos et al. reporting Young's modulus values between 2–6 kPa [41].

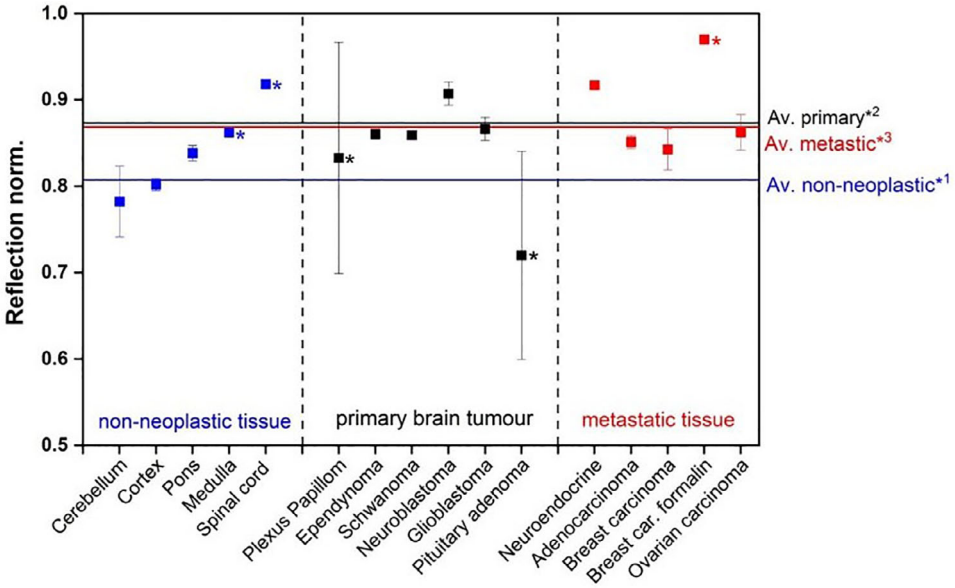

FIGURE 3 | Normalized reflection values for healthy brain tissue, primary tumors, and metastatic tumors at the average tissue weight of 25.7 mg. Horizontal lines indicate the mean reflection of healthy brain tissue (blue), all tumors (red), and primary tumors (black), demonstrating clear separation between tissue classes based on acoustic attenuation. Error bars represent standard deviations of individual measurements. *1 Average brain attenuation includes only soft matter (Cerebellum, Cortex, Pons), *2 Average Primary tumor excludes Plexus Papilloma and Pituitary adenoma, as their consistency has been altered/described as fluid. *3 Average metastasis excludes mamma carcinoma in formalin due to tissue preparation.

Metastatic tumors display intermediate stiffness characteristics, confirming previous shear wave elastography, MR Elastography, and micro indentation-based studies [8, 13, 14, 41]. Fresh mammary carcinoma (0.843 ± 0.024) exhibits reflection values of between non-neoplastic brain and primary brain tumors, aligning with reports of Young's modulus values ranging from 3–7 kPa [13, 17, 40, 45]. However, formalin-fixed mammary carcinoma shows significantly increased stiffness of (0.969 ± 0.004) due to chemical preservation, consistent with previous biomechanical studies showing fixation-induced stiffening of biological tissues [39]. This confirms the known stiffening effect of chemical fixation and validates our decision to exclude preserved samples from comparative analysis. Adenocarcinoma of the lung (0.851 ± 0.008) and neuroendocrine carcinomas (0.917 ± 0.004) exhibit intermediate stiffness profiles, while ovarian carcinoma shows lower stiffness of (0.862 ± 0.021), placing it closer to healthy brain tissue. These findings match previous shear wave elastography analyses, which report variable stiffness in metastatic tumors depending on their origin and microenvironment [14].

The overall comparison of average reflection values highlights clear mechanical differences between tissue types, with non-neoplastic brain tissue showing the lowest average reflection (0.808), metastatic tumors an intermediate reflection (0.868), and primary brain tumors the highest (0.874). These values were calculated while excluding samples altered by surgical treatment or fixation, ensuring a more accurate comparison of intrinsic tissue stiffness. The overall trends confirm that SAW sensing effectively distinguishes between non-neoplastic and tumorous tissues, with primary brain tumors being the stiffest, metastases moderately stiff, and healthy brain the softest. These findings align closely with previous measurements from magnetic resonance elastography, shear wave elastography, and micro indentation techniques, reinforcing the potential of SAW sensing as a non-invasive, real-time tool for intraoperative assessment of tissue stiffness.

3.3 | Implications for Real-Time Diagnostics, Limitations and Future Directions

This study demonstrates the strong potential of SAW sensing as a real-time intraoperative tool for distinguishing tumors from non-neoplastic brain tissue based on their mechanical properties. Providing immediate feedback on tissue stiffness during surgery could assist neurosurgeons in achieving more accurate resections, improving tumor margin identification, and reducing the likelihood of residual tumor cells—especially in eloquent regions. The clear separation observed between non-neoplastic tissue, primary brain tumors, and metastases highlights the suitability of SAW sensing for integration into neurosurgical workflows. Additionally, the differences detected between primary and metastatic tumors suggest that SAW technology could support intraoperative tumor classification, adding valuable biomechanical information alongside existing imaging and visual cues.

While the current study establishes clear and reproducible differences in acoustic attenuation between known tissue classes, a blinded classification of unknown samples was beyond the scope of this proof-of-concept investigation.

Sample numbers for individual tumor types were limited due to clinical availability and ethical constraints. While this restricts statistical power, the consistent trends observed across tissue classes support the robustness of the findings. Future studies will include larger patient cohorts to enable more comprehensive statistical validation.

Future studies will focus on prospective validation using unknown tissue samples, where acoustic measurements will be performed independently of histopathological diagnosis. Subsequent pathological confirmation will enable quantitative assessment of diagnostic performance metrics such as sensitivity, specificity, and classification accuracy. This step will be essential for translating SAW sensing toward clinical decision support.

However, several limitations remain. At present, the system provides relative attenuation values without direct translation into standard mechanical units, such as stiffness measured in kPa. Deriving absolute stiffness values would require additional parameters such as tissue density and wave propagation speed, which may vary across tumor types and physiological conditions. Moreover, this study was conducted ex vivo, where hydration state, temperature, and perfusion are not representative of in vivo environments. Building on the promising results presented, several future developments are envisioned to advance SAW sensing toward clinical application. A critical next step involves material calibration using tissue-mimicking phantoms and hydrogels with known stiffness values to quantitatively correlate SAW attenuation with absolute mechanical properties such as Young's modulus. This will establish a reliable framework for translating acoustic outputs into standard biomechanical units. This will establish a reliable framework for translating acoustic outputs into standard biomechanical units.

In parallel, automated tissue classification using machine learning approaches will be explored to enable real-time decision-making during surgery, using characteristic SAW signal features to distinguish between tissue types. To enhance spatial resolution, high-density SAW arrays could be developed to facilitate stiffness mapping across tumor margins, offering surgeons a visual representation of mechanical gradients at the resection interface. Importantly, future studies will also focus on in vivo validation, assessing the performance of SAW devices in physiologically relevant conditions, where temperature, hydration, and perfusion may influence acoustic wave behavior. These studies will aim to correlate in vivo SAW data with tumor stiffness values measured by established methods such as micro-indentation or shear wave elastography, and with stiffness-matched phantoms.

Despite current limitations, the results presented here establish a strong foundation for the continued development of SAW sensing as a robust, non-invasive intraoperative diagnostic tool with the potential to enhance the safety, precision, and outcomes of brain tumor surgery. Translation to clinical practice will require miniaturization and integration of the SAW system into surgical instruments or flexible probes to enable real-time sensing without interrupting the operative workflow. In future clinical implementations, SAW sensors could be integrated onto the tip of a resection instrument or suction probe to provide real-time, localized stiffness feedback and assist surgeons during tumor removal.

4 | Conclusions

This study demonstrates the potential of surface acoustic wave (SAW) sensing as a real-time, non-invasive tool to differentiate between healthy brain tissue, primary brain tumors, and metastatic tumors based on their mechanical properties. By quantifying acoustic attenuation across a diverse range of tissue types, we observed clear distinctions in stiffness profiles as determined by acoustic attenuation on a reusable SAW sensor, with healthy brain tissue showing the highest attenuation, metastatic tumors intermediate, and primary brain tumors the lowest. These findings closely align with previous biomechanical studies using magnetic resonance elastography, shear wave elastography, and micro indentation, reinforcing the relevance of SAW sensing for intraoperative diagnostics. While further work is needed to calibrate measurements against standard mechanical units and to validate the technology in vivo, this approach provides a promising foundation for improving surgical precision and reducing tumor recurrence through enhanced intraoperative feedback.

Author Contributions

M.E.M. Stamp: Conceptualization, Data curation, Methodology, Validation, Visualization, Formal analysis, Investigation, Writing – Original draft preparation, Project administration, Funding acquisition. **F. Liesche-Starnecker**: Data curation, Investigation, Resources, Writing – Review & Editing. **T. Schaller**: Data curation, Resources, Writing – Review & Editing. **P. Baumgarten**: Surgical sample collection, Resources, Writing – Review & Editing. **N. Lilla**: Surgical sample collection, Resources, Writing – Review & Editing. **D. Mielke**: Surgical sample collection, Resources, Writing – Review & Editing. **D. Collins**: Writing – Review & Editing, Supervision, Funding acquisition.

Acknowledgments

This work was performed in part at the Melbourne Centre for Nanofabrication (MCN) in the Victorian Node of the Australian National Fabrication Facility. This work was supported by a National Health and Medical Research Council (NHMRC) Ideas Grant (ID2003446). Further funding has been provided by a University of Melbourne FEIT Visiting Fellowship and CBE Accelerate Grant Scheme. All work was performed with ethics approval from "Ethikkommission bei der LMU Muenchen" under ethics approval number 24–0338 (title of Project: SOUND—Design of an AI-algorithm for intraoperative tumor recognition using chip-based acoustic signals.

Open access publishing facilitated by The University of Melbourne, as part of the Wiley - The University of Melbourne agreement via the Council of Australasian University Librarians

Conflicts of Interest

The authors declare no conflicts of interest.

Data Availability Statement

The data that support the findings of this study are available from the corresponding author upon reasonable request.

References

1. M. Price, K. Ryan, M. L. Shoaf, et al., "Childhood, Adolescent, and Adult Primary Brain and Central Nervous System Tumor Statistics for Practicing Healthcare Providers in Neuro-Oncology, CBTRUS 2015–2019," *Neuro-Oncology Practice* 11 (2024): 5–25.

2. K. Aldape, K. M. Brindle, L. Chesler, et al., "Challenges to Curing Primary Brain Tumours," *Nature Reviews Clinical Oncology* 16 (2019): 509–520.

3. M. Zetterling, K. Elf, R. Semnic, F. Latini, and E. R. Engström, "Time Course of Neurological Deficits After Surgery for Primary Brain Tumours," *Acta Neurochirurgica* 162 (2020): 3005–3018.

4. B. R. Ecclestone, K. Bell, S. Abbasi, et al., "Improving Maximal Safe Brain Tumor Resection With Photoacoustic Remote Sensing Microscopy," *Scientific Reports* 10 (2020): 17211.

5. C. Bettag, K. Schregel, P. Langer, et al., "Endoscope-Assisted Fluorescence-guided Resection Allowing Supratotal Removal in Glioblastoma Surgery," *Neurosurgical Focus* 50 (2021): 1–7.

6. C. Bettag, A. Hussein, D. Behme, T. Maragkou, V. Rohde, and D. Mielke, "Endoscopic Fluorescence-Guided Resection Increases Radicality in Glioblastoma Surgery," *Operative Neurosurgery* 18 (2020): 41–46.

7. C. Bettag, B. Schatlo, T. Abboud, et al., "Endoscope-Enhanced Fluorescence-Guided Microsurgery Increases Survival in Patients With Glioblastoma," *Acta Neurochirurgica* 165 (2023): 4221–4226.

8. B. H. Duhon, K. Thompson, and M. Fisher, "Tumor Biomechanical Stiffness by Magnetic Resonance Elastography Predicts Surgical Outcomes and Identifies Biomarkers in Vestibular Schwannoma and Meningioma," *Scientific Reports* 14 (2024): 14561.

9. J. M. Bhalodiya, S. N. Lim Choi Keung, and T. N. Arvanitis, "Magnetic Resonance Image-based Brain Tumour Segmentation Methods: A Systematic Review," *Digital Health* 8 (2022): 205520762210741.

10. T. F. Cloughesy, W. K. Cavenee, and P. S. Mischel, "Glioblastoma: From Molecular Pathology to Targeted Treatment," *Annual Review of Pathology: Mechanisms of Disease* 9 (2014): 1–25.

11. I. J. Gerard, M. Kersten-Oertel, J. A. Hall, D. Sirhan, and D. L. Collins, "Brain Shift in Neuronavigation of Brain Tumors: An Updated Review of Intra-Operative Ultrasound Applications," *Frontiers in Oncology* 10 (2021): 618837.

12. A. Šteňo, J. Buvala, V. Babková, A. Kiss, D. Toma, and A. Lysak, "Current Limitations of Intraoperative Ultrasound in Brain Tumor Surgery," *Frontiers in Oncology* 11 (2021): 659048.

13. I. Skambath, J. Kren, P. Kuppler, S. Buschschlueter, and M. M. Bonsanto, "An Attempt to Identify Brain Tumour Tissue in Neurosurgery by Mechanical Indentation Measurements," *Acta Neurochirurgica* 166 (2024): 343.

14. D. Chauvet, M. Imbault, L. Capelle, et al., "In Vivo Measurement of Brain Tumor Elasticity Using Intraoperative Shear Wave Elastography," *Ultraschall in der Medizin—European Journal of Ultrasound* 37 (2016): 584–590.

15. K. Park, G. E. Lonsberry, M. Gearing, A. I. Levey, and J. P. Desai, "Viscoelastic Properties of Human Autopsy Brain Tissues as Biomarkers for Alzheimer's Diseases," *IEEE Transactions on Biomedical Engineering* 66 (2019): 1705–1713.

16. S. Budday, G. Sommer, J. Haybaeck, P. Steinmann, G. A. Holzapfel, and E. Kuhl, "Rheological Characterization of Human Brain Tissue," *Acta Biomaterialia* 60 (2017): 315–329.

17. P. Katira, R. T. Bonnecaze, and M. H. Zaman, "Modeling the Mechanics of Cancer: Effect of Changes in Cellular and Extra-Cellular Mechanical Properties," *Frontiers in Oncology* 3 (2013): 00145.

18. J. Kren, I. Skambath, P. Kuppler, et al., "Mechanical Characteristics of Glioblastoma and Peritumoral Tumor-Free Human Brain Tissue," *Acta Neurochirurgica* 166 (2024): 102.

19. J. Hinrichsen, N. Reiter, L. Bräuer, F. Paulsen, S. Kaessmair, and S. Budday, "Inverse Identification of Region-Specific Hyperelastic Material Parameters for human Brain Tissue," *Biomechanics and Modeling in Mechanobiology* 22 (2023): 1729–1749.

20. M. S. Thomas, "Development of Simple and Portable Surface Acoustic Wave Biosensors for Applications in Biology and Medicine," *Biosignal Processing* (Springer 2022): 106630.

21. D. Peng, W. Tong, D. J. Collins, M. R. Ibbotson, S. Prawer, and M. E. M. Stamp, "Enhanced Effective Diffusion in Sub-Wavelength, Axon-Scale Microchannels Using Surface Acoustic Waves," *Physics of Fluids* 35 (2023): 035101.

22. M. Stamp, A. Jötten, P. Kudella, et al., "Exploring the Limits of Cell Adhesion Under Shear Stress Within Physiological Conditions and Beyond on a Chip," *Diagnostics* 6 (2016): 38.

23. A. Hartmann, M. Stamp, R. Kmeth, et al., "A Novel Tool for Dynamic Cell Adhesion Studies—the De-Adhesion Number Investigator DANI," *Lab on a Chip* 14 (2014): 542–546.

24. M. E. M. Stamp, M. S. Brugger, A. Wixforth, and C. Westerhausen, "Acoustotaxis—In Vitro Stimulation in a Wound Healing Assay Employing Surface Acoustic Waves," *Biomaterials Science* 4 (2016): 1092–1099.

25. Y. Huang, P. K. Das, and V. R. Bhethanabotla, "Surface Acoustic Waves in Biosensing Applications," *Sensors and Actuators Reports* 3 (2021): 100041.

26. T. Wang, R. Green, R. Nair, et al., "Surface Acoustic Waves (SAW)-based Biosensing for Quantification of Cell Growth in 2D and 3D Cultures," *Sensors* 15 (2015): 32045–32055.

27. D. Mandal and S. Banerjee, "Surface Acoustic Wave (SAW) Sensors: Physics, Materials, and Applications," *Sensors* 22 (2022): 820.

28. Y. Wu, A. G. Stewart, and P. V. S. Lee, "On-Chip Cell Mechanophenotyping Using Phase Modulated Surface Acoustic Wave," *Biomicrofluidics* 13 (2019): 24107.

29. H. Wu, H. Zu, J. H. C. Wang, and Q. M. Wang, "A Study of Love Wave Acoustic Biosensors Monitoring the Adhesion Process of Tendon Stem Cells (TSCs)," *European Biophysics Journal* 48 (2019): 249–260.

30. A. Ruland, X. Chen, A. Khansari, et al., "A Contactless Approach for Monitoring the Mechanical Properties of Swollen Hydrogels," *Soft Matter* 14 (2018): 7228–7236.

31. A. Ruland, C. Onofrillo, S. Duchi, C. Di Bella, and G. G. Wallace, "Standardised Quantitative Ultrasound Imaging Approach for the Contact-less Three-dimensional Analysis of Neocartilage Formation in Hydrogel-based Bioscaffolds," *Acta Biomaterialia* 147 (2022): 129–146.

32. M. E. M. Stamp, M. Halwes, L. Caballero Aguilar, K. Callaghan, D. Nisbet, and D. Collins, *Non-Destructive Surface Acoustic Wave Sensing for Real-Time Material Characterisation of Gelma Hydrogels*, (Elsevier, 2025).

33. V. M. Gerganov, A. Samii, A. Akbarian, L. Stieglitz, M. Samii, and R. Fahlbusch, "Reliability of Intraoperative High-Resolution 2D Ultrasound as an Alternative to High–Field Strength MR Imaging for Tumor Resection Control: A Prospective Comparative Study," *Journal of Neurosurgery* 111 (2009): 512–519.

34. K. Tamura, K. Ito, S. Yoshida, J. Mamou, K. Miura, and S. Yamamoto, "Alteration of Speed-of-Sound by Fixatives and Tissue Processing Methods in Scanning Acoustic Microscopy," *Frontiers in Physics* 11 (2023): 1060296.

35. G. Singh and A. Chanda, "Mechanical Properties of Whole-body Soft human Tissues: A Review," *Biomedical Materials* 16 (2021): 062004.

36. A. G. Bhargav, J. S. Domino, R. Chamoun, and S. M. Thomas, "Mechanical Properties in the Glioma Microenvironment: Emerging Insights and Theranostic Opportunities," *Frontiers in Oncology* 11 (2022): 805628.

37. M. Meyer, N. Bouchonville, C. Gaude, E. Gay, D. Ratel, and A. Nicolas, "The Micromechanical Signature of Pituitary Adenomas: New Perspectives for the Diagnosis and Surgery," *Advanced NanoBiomed Research* 1 (2021): 2000085.

38. C. Hahn and M. A. Schwartz, "Mechanotransduction in Vascular Physiology and Atherogenesis," *Nature Reviews Molecular Cell Biology* 10 (2009): 53–62.

39. H.-J. Wilke, S. Krischak, and L. E. Claes, "Formalin Fixation Strongly Influences Biomechanical Properties of the Spine," *Journal of Biomechanics* 29 (1996): 1629–1631.

40. D. C. Stewart, A. Rubiano, K. Dyson, and C. S. Simmons, "Mechanical Characterization of human Brain Tumors From Patients and Comparison to Potential Surgical Phantoms," *PLoS ONE* 12 (2017): e0177561.

41. C. Harkos, S. F. Svensson, K. E. Emblem, and T. Stylianopoulos, "Inducing Biomechanical Heterogeneity in Brain Tumor Modeling by MR Elastography: Effects on Tumor Growth, Vascular Density and Delivery of Therapeutics," *Cancers* 14 (2022): 884.

42. M. Khoonkari, D. Liang, M. Kamperman, F. A. E. Kruyt, and P. van Rijn, "Physics of Brain Cancer: Multiscale Alterations of Glioblastoma Cells Under Extracellular Matrix Stiffening," *Pharmaceutics* 14 (2022): 1031.

43. C. C. Parkins, J. H. McAbee, L. Ruff, et al., "Mechanically Matching the Rheological Properties of Brain Tissue for Drug-Delivery in Human Glioblastoma Models," *Biomaterials* 276 (2021): 120919.

44. W. Chemaitilly, G. T. Armstrong, A. Gajjar, and M. M. Hudson, "Hypothalamic-Pituitary Axis Dysfunction in Survivors of Childhood CNS Tumors: Importance of Systematic Follow-Up and Early Endocrine Consultation," *Journal of Clinical Oncology* 34 (2016): 4315–4319.

45. A. Massey, J. Stewart, C. Smith, et al., "Mechanical Properties of Human Tumour Tissues and Their Implications for Cancer Development," *Nature Reviews Physics* 6 (2024): 269–282.

46. C. Bettag, A. Hussein, B. Schatlo, et al., "Endoscope-Assisted Visualization of 5-Aminolevulinic Acid Fluorescence in Surgery for Brain Metastases," *Journal of Neurosurgery* 137 (2022): 1650–1655.